Spectroscopic Measurements of Oxygen Saturation in the Retina

Jessica C. Ramella-Roman and Scott A. Mathews, *Member, IEEE*

***Abstract*—We introduce a new type of retinal oximeter able to capture multiple spectroscopic sensitive images of the retina in a single snapshot. The core of our apparatus is a multiaperture camera that can be easily interfaced with a fundus camera system. A lenslet array divides the image collected by a fundus camera into identical subimages. A bandpass filter array in front of the lens system is used to collect the subimages only at the wavelengths of interest. Two different instruments were designed based on this simple principle. The first system can collect six different images, while the second system can collect up to 18 different images in a single snapshot.**

***Index Terms*—Image registration, optical spectroscopy.**

I. Introduction

THE DETERMINATION of optical properties in the human eye is a complex task. The eye is a multilayered structure encompassing many absorbing and scattering materials [1]. There is great interest in determining oxygen saturation in the retina vessels, since these values can be useful in determining early retina pathologic changes [2]. Variations in blood flow and retina autoregulation have been linked to the onset of diabetic retinopathy [3], visual loss [4], and significant decrease in an individual quality of life. Recent studies [2] have shown that macular edema can be reduced by supplementing oxygen to patients, it is then important to develop minimally invasive tools for the measurement of oxygen saturation in the retina to monitor DR progress.

The goal of our study is the construction of a retinal oximeter that is able to assess oxygen saturation in the vessel of the retina to investigate early changes in the eye due to diabetic retinopathy.

Retinal oximeters have been designed and built for more than 40 years [5]. Most systems use a fundus camera to access the eye illuminating the retina at different wavelengths and, rely on the characteristic shape of the hemoglobin absorbance spectrum to calculate the oxygen content.

Hickam *et al*. in 1963 [6] designed a two-wavelengths system that used a film camera and narrow-band filters. The filters were either the doublet 640 and 800 nm or 640 and 505 nm. (Both 815 and 505 nm are hemoglobin isobestic points.) They concluded that oxygen saturation in the retina veins was 58% $\pm 10\%$.

In 1975, Pittman *et al*. showed that by using three wavelengths, more accurate measurements could be obtained [7], since the scattering from red blood cells and other structures could then be taken into account. Delori [8] used three wavelengths in his retinal oximeter (558, 569, and 586 nm). The wavelengths were chosen to maintain high vessel to background contrast and to reduce the impact of light scattering in the ocular media and vessel walls. Schweitzer *et al*. [9] designed a point measurement retinal oximeter. The sampling band was between 400 and 700 nm with 2 nm intervals. Values between 510 and 586 nm were used for calculating oxygen saturation. Their measurement predicted $92.2\% \pm 4.1\%$ oxygen saturation in retinal arteries and $57.9\% \pm 9.9\%$ in veins. A scanning mechanism was then added to obtain small images of retinal vessels.

Denninghoff *et al*. [10] used two laser diodes at 670 and 830 nm respectively to calculate oxygen content in the retina. Their system did not use a fundus camera [12], [13] and was tested on swines during controlled hemorrhage. Similarly Drewes used a confocal system combined with four laser lines [11] to obtain SO_2 values in small regions of the retina, the system could scan across a retina vessel and give information about vessel size and oxygen saturation.

Recently, Johnson *et al*. [14] have introduced a hyperspectral imager based on a fundus camera that is able to collect 50 spectroscopic sensitive images of the retina. Their system uses a diffractive grating that creates an array of images on a charge-coupled device (CCD). Oxygen saturation values across large portions of the retina are obtained with a Monte Carlo based model.

In this paper, we illustrate two retinal oximeters based on a lenslet array design. Similarly to the method of Johnson, we divide the image obtained with the fundus system into several wavelength sensitive images. The first system is able to collect six images at six different wavelengths by using an inexpensive camera; the second imager can generate eighteen images and is based on a large-format camera. We are interested in studying not only the oxygen content in the retina, but also quantifying the different eye chromophores, therefore a high number of measuring wavelengths is desirable.

II. Light Transport in the Retina Layers

The eye is composed of several layers, each different in structure, absorption and scattering properties. The optical properties of these layers determine the total amount of light retroreflected by the eye fundus as well as the light spectral shape. Effective models for the calculation of oxygen saturation in the retina try to compensate for the effect of the various layers, ultimately isolating the absorption due the superficial retina vessels. In this section we will use Monte Carlo simulations to model the behavior of light traveling through the retina. First we will show the impact of choroidal melanin on the retro-reflected beam as

Manuscript received September 23, 2007. This work was supported in part by the Wallace H. Coulter Foundation.

The authors are with the Catholic University of America, Washington, DC 20064 USA (e-mail: ramella@ cua.edu; mathews@cua.edu).

Digital Object Identifier 10.1109/JSTQE.2007.911312

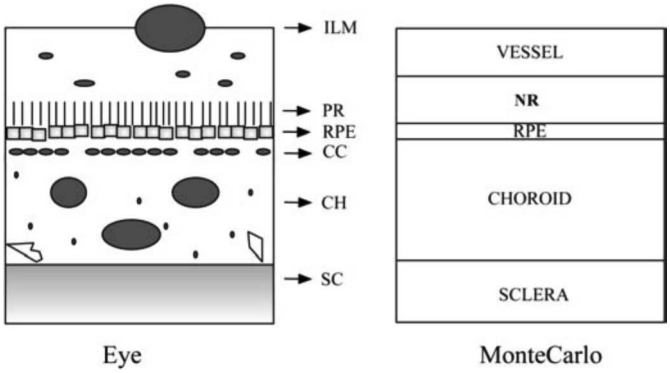

Fig. 1. Layers in the ocular fundus (left) are simplified in Monte Carlo simulations (right). Retinal vessel can be as little as 10 μm and as large as 250 μm. The layer starting with the inner limiting membrane (ILM) and ending with the photoreceptors (PR) is the NR. The retinal-pigmented epithelium is a 10-μm thick-layer; the main absorber in this layer is melanin. Choriocapillaris (CC) and choroidal stroma (CH) are considered the large layer of the choroid, where main absorbers are melanin and blood. Finally, the sclera is 700 μm thick (not to scale in the graph), and is composed, in large part, of collagen fibrils.

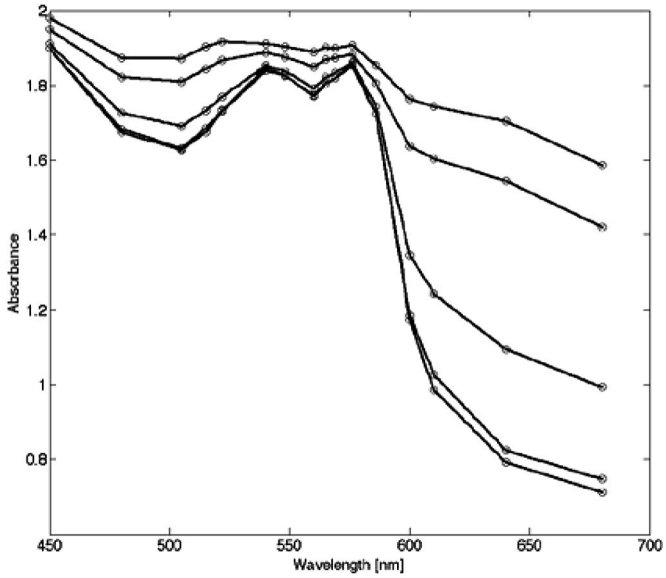

Fig. 2. Monte Carlo model of retinal tissue when the choroids melanin is increased from 0.001 to 10 mmol $\cdot$ l^{-1}. The top curve (higher absorbance) corresponds to a melanin concentration of 10 mmol $\cdot$ l^{-1}.

a function of wavelength. Secondarily we will evaluate the error in the calculation of oxygen saturation in superficial retinal vessels induced by the choroidal pigmentation.

In Fig. 1 we show the layout of the ocular fundus as well as a simplified representation used in the Monte Carlo simulations. Superficial retina vessels can be large (up to 250 μm in diameter for veins, 150 μm for arteries), highly scattering due to the presence of erythrocytes, and absorbing because hemoglobin has high extinction coefficient [1]. Retina vessels are surrounded by the neural retina; this layer is ca. 200 μm thick and includes the photoreceptors. The next layer is the retinal pigmented epithelium, a one-cell layer 10 μm thick and highly pigmented. The choroid is a complex 250-μm-thick structure comprising large blood vessels, melanocytes, and connective tissues including collagen. Finally, the sclera is a 700-μm-thick layer composed of collagen fibrils (type I and type III); highly scattering the sclera exerts little absorption.

Several authors have modeled light transport through the retina. Hammer *et al*. [15], and Preece and Claridge [16] used the MCML program [17] to show the impact of the various retina layers on the retroreflected light. Hammer *et al*. measured the optical properties of the cow retina by using a double integrating sphere layout, and then, used the properties in Monte Carlo and adding doubling simulations [18]. Preece and Claridge modeled four retina layers in their Monte Carlo simulations. They considered the neural retina, the choroids, the retinal pigment epithelium (RPE), and the sclera. They used Hammer's scattering coefficients (μ_s) for all layers, reducing the neural retina μ_s to 25% of the value proposed by Hammer to simulate human retina values. The tissue anisotropy (g) was considered constant across all the wavelengths by most groups [15], [16]. We also decided to use this approximation since g varies only of a few percent in the range of interest [21]. The main absorbers in the retina are oxygenated (HbO_2), deoxygenated hemoglobin (Hb) (in the retina vessel, choroid), and melanin (in the RPE, choroid). Values of melanin absorption coefficients were obtained from Anderson and Parrish [19].

The extinction coefficients of Hb and HbO_2 have been tabulated [20], and are available at most visible wavelengths. The choroid total absorption coefficient is a combination of melanin and hemoglobin absorptions. The choroid is considered 95% oxygenated with a 70% blood volume fraction. Values of melanin concentration vary depending on the patient eye color and ethnicity [1]. In our simulations, the melanin concentration varied from 0.001 to 10 mmol $\cdot$ l^{-1}, while the blood content was kept at the aforementioned values. The RPE melanin concentration was 1 mmol $\cdot$ l^{-1}. Choroid pigmentation has been shown to influence the total reflectance from the retina [16]; this effect is shown in Fig. 2.

Four retina layers were used in this simulation, the neural retina, the RPE, the choroid, and the sclera. All simulations were conducted with MCML and 1 million photons. Twenty different wavelengths, uniformly distributed between 450 and 680 nm, were considered. The optical properties used in this simulation are the same as in [16].

The impact of choroidal melanin is most visible at larger wavelengths; for this reason, some authors [21] have chosen models that use reflectance values in the green region of the spectrum. The RPE concentration varies among different individuals, but its effect is less wavelength-dependent; hence, it is easier to eliminate.

In a second simulation, we assessed the efficacy of two models of oxygen saturation in the top retina vessels as choroidal melanin changes. The algorithms were as follows: a three-wavelength model by Delori [21] and a multiwavelengths algorithm by Schweitzer *et al*. [9].

In this simulation, we considered five retina layers, the four layers previously mentioned with the addition of a top vessel. To model the vessel optical properties, we used values of

whole blood measured by Gemert *et al.* [22]. In their calculation, the scattering coefficient of oxygenated blood differs from the one of deoxygenated blood, as well as the respective absorption coefficients. Anisotropy was kept constant at 0.99, although it is known to vary between 0.993 and 0.998 across the wavelengths of interest. Although the Henyey-Greenstein phase function used in MCML is not optimal when describing light scattering from red blood cells it is a good approximation. Blood absorption in the superficial vessels dominates scattering ($\mu_a >> \mu_s$'), moreover the simulations were conducted on a retinal vessel whose diameter is 10 μ so than less than one scattering event occurs within the vessel boundaries. Keeping the neural retinal layer may seem redundant, but Hammer suggested in his paper [18] that the measurement of the neutral retina (NR) layer does not always included retinal vessels; in fact, the values of absorption of this layer are several orders of magnitude smaller than the one expected for blood. Simulations conducted on a 10 μm vessels are shown in Figs. 3 and 4, simulations conducted on larger vessels showed a similar behavior.

Oxygen saturation in the top retinal vessel was varied between 0 and 100%. The simulations were conducted for different values of choroidal melanin concentrations. The reflectance values obtained with the five-layer model I_{ves} were normalized by values obtained without the vessel I_{std}; this mimics what is commonly done experimentally, where the reflectance data on the vessel are normalized by reflectance values near to the vessel.

We first tested a three-wavelength algorithm proposed by Delori *et al.* [21]. In the first model, oxygen saturation is obtained with the following equation:

$$\mathrm{SO}_2 = \left(D^{\lambda 1}\left(\varepsilon_{\text{Hb}}^{\lambda 3} - \varepsilon_{\text{Hb}}^{\lambda 2}\right) + D^{\lambda 2}\left(\varepsilon_{\text{Hb}}^{\lambda 1} - \varepsilon_{\text{Hb}}^{\lambda 3}\right) + D^{\lambda 3}\left(\varepsilon_{\text{Hb}}^{\lambda 2} - \varepsilon_{\text{Hb}}^{\lambda 1}\right)\right) \Big/ \left(\begin{array}{c} D^{\lambda 1}\left[\left(\varepsilon_{\text{Hb}}^{\lambda 3} - \varepsilon_{\text{HbO}_2}^{\lambda 3}\right) - \left(\varepsilon_{\text{Hb}}^{\lambda 2} - \varepsilon_{\text{HbO}_2}^{\lambda 2}\right)\right] \\ + D^{\lambda 2}\left[\left(\varepsilon_{\text{Hb}}^{\lambda 1} - \varepsilon_{\text{HbO}_2}^{\lambda 1}\right) - \left(\varepsilon_{\text{Hb}}^{\lambda 3} - \varepsilon_{\text{HbO}_2}^{\lambda 3}\right)\right] \\ + D^{\lambda 3}\left[\left(\varepsilon_{\text{Hb}}^{\lambda 2} - \varepsilon_{\text{HbO}_2}^{\lambda 2}\right) - \left(\varepsilon_{\text{Hb}}^{\lambda 1} - \varepsilon_{\text{HbO}_2}^{\lambda 1}\right)\right] \end{array}\right)$$

where $D = -\log\ 10(I_{\text{ves}}/I_{\text{std}})$, and $\varepsilon_{\text{HbO}_2}$ and ε_{Hb} are tabulated values of the extinction coefficient for oxygenated and deoxygenated hemoglobin [20].

Results obtained with the three-wavelength algorithm are shown in Fig. 3.

The three-wavelengths algorithm is able to reconstruct the true values of oxygen saturation of the outer retinal vessel but some errors are present. At low SO_2 values the error is large, similarly low choroidal melanin concentrations show a significant error. Experimentally high values of melanin in the choroid lead to higher error due to the low level of light back-reflected from the retina, but in the simulations the presence of melanin in the choroid attenuates the effect of blood absorption and scattering in that layer.

A second multiwavelength model introduced by Schweitzer is particularly effective when large number of wavelengths are available. The algorithm keeps into account not only the hemoglobin absorption but also the wavelength-dependent scattering of erythrocytes. The optical density of light backscattered from a vessel is modeled as

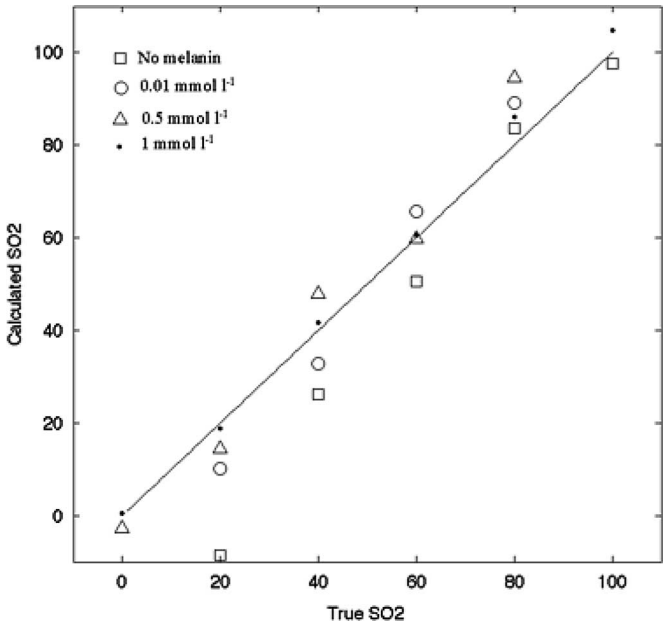

Fig. 3. Oxygen saturation in a 10 μm retinal vessel obtained with a three-wavelength algorithm for four different values of choroidal melanin.

$$D(\lambda) = B + n\ \log\left(\frac{1}{\lambda}\right) + b[\varepsilon_{\text{Hb}}(\lambda) + s(\varepsilon_{\text{HbO}_2}(\lambda) - \varepsilon_{\text{Hb}}(\lambda))]c_{\text{tot}}l$$

where the first two terms B and $n\log(1/\lambda)$ are used to simulate both wavelength-independent and wavelength-dependent scattering. The term s is an experimental geometry factor, c_{tot} is the total hemoglobin concentration, and l is the vessel thickness.

A least squares mechanism using the Nelder–Mead simplex method [23] is in combination with *four* fitting parameters (B, $A = c_{\text{tot}}^{lb}$, s, and n). Results obtained with this model using 14 wavelengths uniformly distributed between 450 nm and 700 nm are shown in Fig. 4.

The algorithm is effective in capturing true values of oxygen saturation in the retina vessel, although better results are again obtained when some melanin is present in the choroid and at high SO_2 values. A minimization technique such as the one necessary for the multiwavelengths algorithm is dependent on initial values and is time-consuming. Nevertheless, this type of algorithm offers more information regarding the eye structure. This can be useful when assessing retina spatial variability. We have used both models in our experimental work.

III. Multiaperture Camera

A. Fundus Spectral Imager

We built an experimental apparatus for the measurement of oxygen saturation in the retina. The system is based on a fundus camera (TRC-FET, Topcon Paramus, NJ). Fundus cameras or retinal cameras are common instruments in ophthalmic clinics

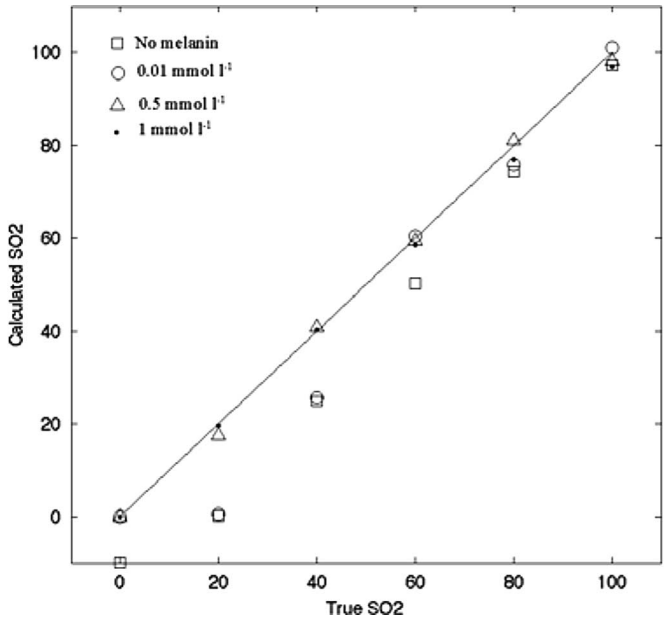

Fig. 4. Oxygen saturation in a 10 μm retinal vessel obtained with a multiwavelength algorithm for four different values of choroidal melanin.

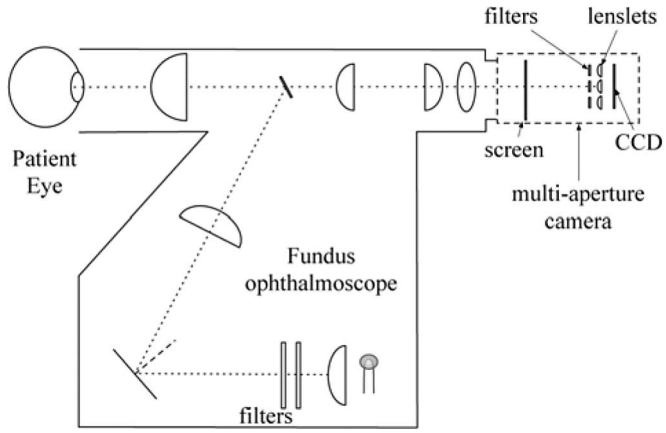

Fig. 5. Modified fundus camera for retinal oxygenation measurements.

and provide a magnified view of the patient retina. The imager in the fundus system was replaced with a multiaperture camera so that a minimum of 6 and a maximum of 18 retinal images could be collected in a single snapshot. A layout of the system is shown in Fig. 5. The fundus camera contains a xenon lamp continuous light source as well as a flash that can be triggered by the multiaperture camera. We used the dc light source in most of the experiments. The multiaperture camera could be attached at the exit pupil of the fundus system in place of the original film camera. Images were collected in a dark room.

B. Six-Lens Camera System

Our first system was based on a six-lens array [15]. The system consisted of a 10 bit monochromatic digital camera (Lumenera, North Andover, MA) combined with a lenslet array and a filter array. The camera CCD size was 10.2 mm $\times$ 8.3 mm with 1392 pixels $\times$ 1040 pixels. The lenslet array was custom built with six plano-convex lenses (LightPath Optical Instrumentation, Shanghai, China) supported by an aluminum plate. The lenses were 2 mm in diameter and had an aperture equal to 0.15 and an effective focal length of 5 mm. Lens to lens separation was 2.5 mm. The bandpass filters [20 nm full-width at half maximum (FWHM)], Newport, Irvine, CA) were arranged in a layout similar to the lenslet array, each filter was 2.5 mm $\times$ 2.5 mm, only the 575 nm filter was circular with a 3 mm diameter. Different combinations of filter arrays were tested including the quintuplet [540, 560, 576, 600, 680] nm, and the sextuplets [560, 575, 600, 630, 650, 660] nm and [540, 560, 575, 600, 650, 660] nm. The filters were positioned at 0.2 mm from the lenses. Fig. 2 illustrates the concept of image multiplication achieved with the multiaperture camera. The letter F is projected onto a screen (CCD) camera through six equally spaced lenses. The ray tracing of the optical system was obtained with the software package Rayica (Optica Software, Champaign, IL).

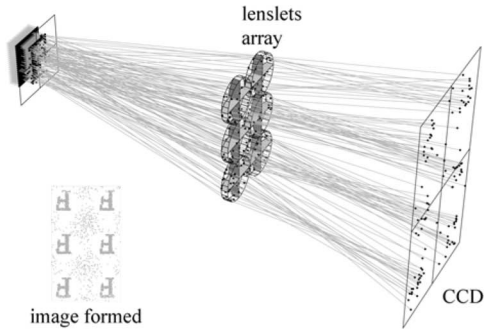

Fig. 6. Image division with a lenslet array; the inset shows the resulting image.

After registration the largest image obtainable with this system is 300 pixels $\times$ 300 pixels, images with higher resolution are desirable especially when observing small retina capillaries.

C. 18-Lens Camera System

When using models for the calculation of SO_2 and optical properties in the retina such as the one by Schweitzer a large number of wavelengths is desirable. We have built an imaging system that can accommodate 18 separate images on a single CCD. The system uses a 12 b monochromatic digital camera (Lumenera, North Andover, MA) whose CCD is 36.1 mm $\times$ 24.0 mm and 4008 pixels $\times$ 2672 pixels. A lenslet array was designed to maximize each subimage area; the lens layout is shown in Fig. 7. Horizontally, each lens was 0.6 cm center to center, while in the vertical direction lens, center to center separation was 1 cm. Multielement glass lens (Sunex, Carlsbad, CA) with focal length of 5.9 mm were used in this system. The lenses were encased in a black plastic support. A filter array with identical layout was positioned in front of the lenses array. The filter array was composed of 14 color filters (20 nm FWHM, Newport, Irvine, CA), three polarizers (Edmund Optics, Barrington, NJ), and one neutral density filter (OD = 0.3, Edmund Optics, Barrington, NJ).

The color filters were, respectively, 460, 480, 500, 520, 530, 540, 560, 580, 590, 600, 620, 630, 640, and 660 nm. The three polarizers were oriented respectively at 0°, 45°, and 90° to the

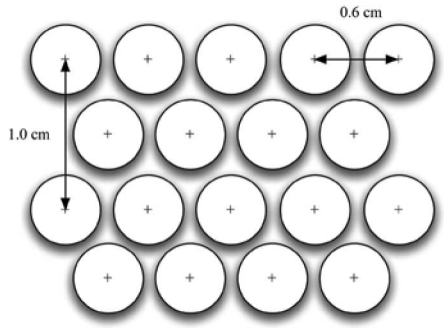

Fig. 7. Layout of the lenslet array for the large-format camera.

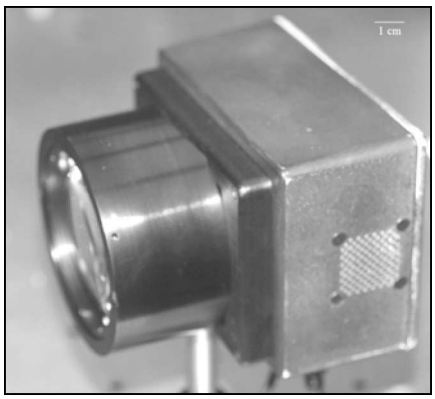

Fig. 8. Large-format multiaperture camera.

source polarization. By combining the images obtained with the three polarizers and the ND filter, we can obtain the first three terms of the Stokes vector. The Stokes vector can give us an idea of structural features in the eye; this work will not be presented here.

In order to minimize the effect of lens parallax on the resulting image, two large ($\mathrm{diameter} = 6\,\mathrm{cm}$) magnifying lenses ($f = 150\,\mathrm{mm}$) were positioned in front of the filters and lenses array. The system was enclosed in a black anodized aluminum case. A photo of the complete imager is shown in Fig. 8.

By using this combination, the multiaperture system focal length was 3 cm and field of view was 3 cm $\times$ 3 cm. The largest obtainable images with this system were 600 pixels $\times$ 600 pixels.

D. Systems Calibration

Both camera spectral responses were tested with the aid of colored National Institute of Standards and Technology (NIST) traceable Spectralon standard (Labsphere, North Sutton, NH). The standards were green and yellow. Images of the standard were captured with our modified fundus camera system, and then, normalized by a 90% reflectance standard that was also NIST traceable. Results obtained with the 18-lens system are shown in Fig. 9. The six-lens system gave very similar results, since the same type of filters are used in both cameras. The imager was used to measure the reflectance from the solution of hemoglobin. A total of 25 mg of bovine hemoglobin (Sigma, St. Louis, MO) was dissolved in 200 mL of water, the solution was left in open air for several minutes to allow the hemoglobin to

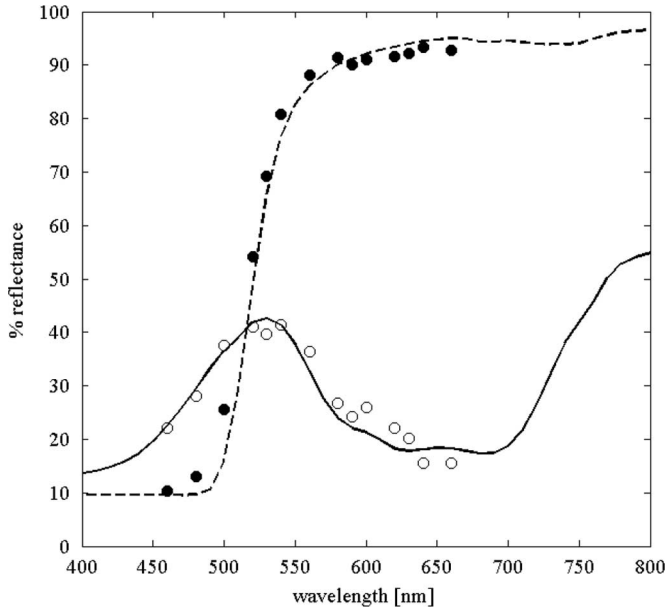

Fig. 9. Normalized reflectance from color standards, obtained with the 18-lens system (only 14 color filters are used). The filled symbols are experimentally obtained values of reflectance from a green standard normalized by a 90% reflectance standard. The filled symbols are values obtained with the yellow standard. The lines are the corresponding calibrated values of reflectance given by the manufacturer.

completely dissolve and bind with oxygen. The liquid assumed a brownish red color, and was then, stored in a 1-cm-thick plastic cuvette. The absorbance of the hemoglobin filled cuvette was measured with a bench-top spectrophotometer (Ultrospec 3000, Pharmacia Biosystems, DK). Typical shapes of oxyhemoglobin were obtained (see Fig. 10). Half of the mixture was then combined with 5 mg of sodium hydrosulfite (Sigma, St Louis, MO), and stored in a 1-cm-thick plastic cuvette. Sodium hydrosulfite is a reducing agent and was used to deoxygenate the hemoglobin solution. The cuvette was sealed to avoid hemoglobin recombination with oxygen. The mixture was measured with the spectrophotometer and showed a typical deoxyhemoglobin absorption curve, Fig. 10. Finally, both cuvette were positioned at 3 cm from the large multiaperture imager.

A white led source (Throlabs, Newton, NJ) was positioned behind the cuvettes facing the imager; a diffuser was added in between the cuvettes and the light source. Fourteen wavelength-sensitive images of light transmitting through the cuvette were obtained in a single snapshot. In the inset of Fig. 10, we show three of such images, for 500, 560, and 600 nm, respectively. Two 100 $\times$ 100 pixels regions were selected on each image, one on the cuvette containing oxygenated hemoglobin and one on the cuvette containing deoxygenated hemoglobin.

The average value of transmission (T) through such regions was calculated and then transformed into absorbance (A) values using the equation

$$A = -\frac{1}{L}\log_{10}(T) \tag{1}$$

where L is the cuvette thickness (1 cm). The results were compared with the spectrophotometer measurements. Both curves

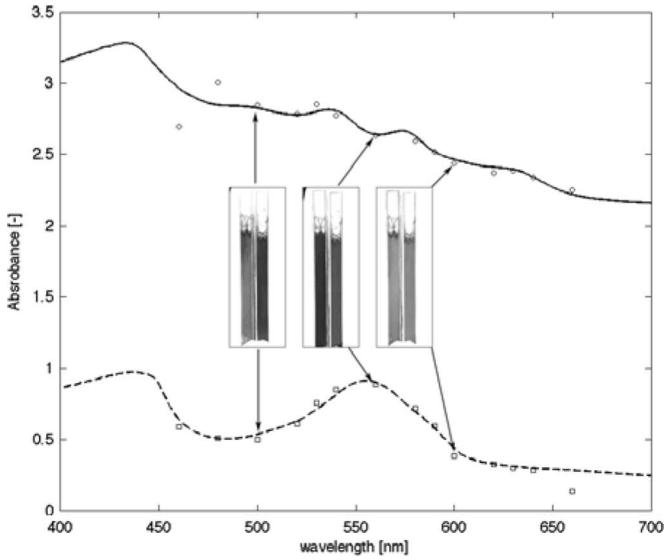

Fig. 10. Absorption of bovine hemoglobin obtained with the multispectral camera. The cuvette on the left contains deoxygenated hemoglobin; the right cuvette contains oxygenated hemoglobin. The lines correspond to values obtained with a bench-top spectrophotometer, and the circles correspond to values obtained averaging region of interest in the cuvette images. From the viewer left to right, the images correspond to 500, 560, and 600 nm, respectively. As absorbance decreases, more light is allowed to pass through the cuvette. The oxyhemoglobin curve is shifted (+2) for clarity.

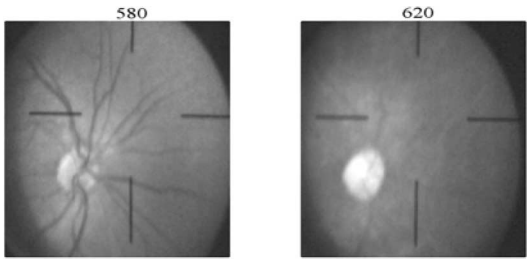

Fig. 11. Images obtained with the large-format imager showing the difference in absorbance of the retinal vessels. At 580 nm, the vessels are clearly visible, while at 620 nm, they have disappeared due to the low hemoglobin absorption.

were normalized by their maximum value. The curves show agreement between the curves measured with the spectrophotometer and the values obtained with the multi-aperture imager.

Similar experiments were also conducted with the six-lens system [23], using cuvettes as well as a simplified model of the human eye. The data were modeled with both Delori [11] and Schweitzer [12] algorithms; values of oxygen saturation were obtained with an associated error of ca. 10%.

IV. Results

Both systems were tested on the eyes of healthy volunteers. The subject's right eye was dilated with tropicamide ophthalmic solution (Akorn, Inc., Buffalo Grove, IL), 20 min before testing. The process then followed the procedure of a clinical fundus exam.

Oxygen saturation values on selected vessels of the retina were obtained following the Shweitzer's algorithm. Arteries and veins were identified on the images, then regions of interest were selected on the vessel area (R_{vessel}) and in regions in close proximity to the vessel ($R_{\text{background}}$). The average pixel values captured on the vessel where normalized by that next to it. The optical density of the vessel region was calculated as

$$\text{OD}\,(\lambda) = -\log_{10}\left(\frac{R_{\text{vessel}}\,(x,y,\lambda)}{R_{\text{background}}\,(x,y,\lambda)}\right). \qquad (2)$$

Average values of oxygen saturation were 95% for arteries and 0.54% for veins. Although the large-format camera allows for the collection of more data point than the six-lenslet system, we experienced a similar level of variability in the measurement. Values of oxygen saturation varied of up to 10% across the same vessel depending on its position. Part of the variability is possibly due to the nonuniformity of the eye absorber, but we believe that a more accurate model is necessary to capture the complex eye structure. The 18-lens imager was built with this purpose in mind.

V. Conclusion

We have introduced a new type of imaging system based on the spectroscopic and spatial division of a fundus image. The system is particularly suited for imaging the eye for its ability to collect all the images in a single snapshot. Projecting images onto a CCD necessarily decrease each image resolution. Our original system was able to collect six 300 pixels $\times$ 300 pixels images, using a large-format camera, we are now able to collect up to 18 images twice as big. Unfortunately, large-format CCDs are still relatively expensive and slow. The real difficulty of this measurement is in the calculation of oxygen saturation value that can be trusted. In our Monte Carlo simulations we have shown how the presence of melanin in the choroids impacts the calculation of oxygen saturation for two typical models. The 14 wavelengths algorithm shows lower error than the 3 wavelengths model but is dependent on initial values and is slow hence unpractical in an imaging environment. Other techniques such as Monte Carlo are showing promising results [14], but they are slow and are easily fooled by imaging artifacts. One of our aims in constructing this system is to investigate parametric models of light travel into the retina. We believe that our 18-lens system will be very useful for this purpose.

Acknowledgment

The authors want to thank A. Nabili for his help in the testing phase of the 18-lens system.

References

[1] R. Snell and M. A. Lemp, *Clinical Anatomy of the Eye*. Oxford, U.K.: Blackwell, 1998.

[2] Q. D. Nguyen, S. M. Shah, E. van Anden, J. U. Sung, S. Vitale, and P. A. Campochiaro, "Supplemental oxygen improves diabetic macular edema: A pilot study," *Invest. Opthalmol. Vis. Sci.*, vol. 45, pp. 617–624, 2004.

[3] E. M. Kohner, V. Patel, and S. M. Rassam, "Role of blood flow and impaired autoregulation in the pathogenesis of diabetic retinopathy," *Diabetes*, vol. 44, pp. 603–607, 1995.

[4] N. D. Wangsa-Wirawan and R. A. Linsenmeier, "Retinal oxygen: Fundamental and clinical aspects," *Arch. Ophthalmol.*, vol. 121, pp. 547–557, 2003.

[5] A. Harris, L. Dinn, R. B. Kagemann, and E. Rechtman, "A review of methods for human retinal oximetry," *Ophtalmic Surg., Laser Imag*., vol. 34, pp. 152–164, 2003.
[6] J. B. Hickam, R. Frayser, and J. C. Ross, "A study of retinal venous blood oxygen saturation in human subjects by photographic means," *Circulation*, vol. 27, pp. 375–385, 1963.
[7] R. N. Pittman and B. R. Duling, "A new method for the measurement of percent hemoglobin," *J. Appl. Physiol*., vol. 38, pp. 315–320, 1975.
[8] F. C. Delori, "Noninvasive technique for oximetry of blood in retina vessels," *Appl. Opt*., vol. 27, pp. 1113–1125, 1988.
[9] D. Schweitzer, L. Leistritz, M. Hammer, M. Scibor, U. Bartsch, and J. Strobel, "Calibration-free measurement of the oxygen saturation in retinal vessel of men," in *Proc. SPIE Ophthalmic Technol. V*, 1995, vol. 2393, pp. 210–218.
[10] K. R. Denninghoff, M. H. Smith, R. A. Chipman, L. W. Hillman, P. M. Jester, C. E. Hughes, F. Kuhn, and L. W. Rue, "Retinal large vessel oxygen saturation correlates with early blood loss and hypoxia in anesthetized swine," *J. Trauma*, vol. 43, pp. 29–34, 1997.
[11] J. J. Drewes, M. H. Smith, K. R. Denninghoff, and L. W. Hillman, "An instrument for the measurement of retinal vessel oxygen saturation," *Proc. SPIE*, vol. 3591, pp. 114–120, 1999.
[12] K. R. Denninghoff, M. H. Smith, A. Lompado, and L. W. Hillman, "Retinal venous oxygen saturation and cardiac output during controlled hemorrhage and resuscitation," *J. Appl. Physiol*., vol. 94, pp. 891–896, 2003.
[13] W. R. Johnson, D. W. Wilson, W. Fink, M. Humayun, and G. Bearman, "Snapshot hyperspectral imaging in ophthalmology," *J. Biomed. Opt*., vol. 12, pp. 14036–14043, 2007.
[14] M. Hammer, A. Roggan, D. Schweitzrt, and G. Muller, "Optical properties of ocular fundus tissues—An in vitro study using the double-integrating-sphere technique and inverse Monte Carlo simulation," *Phys. Med. Biol*., vol. 40, pp. 963–978, 1995.
[15] S. J. Preece and E. Claridge, "Monte Carlo modeling of the spectral reflectance of the human eye," *Phys. Med. Biol*., vol. 47, pp. 2863–2877, 2002.
[16] L. H. Wang, S. L. Jacques, and L. Q. Zheng, "MCML—Monte Carlo modeling of photon transport in multilayered tissues," *Comput. Methods Programs Biomed*., vol. 47, pp. 131–146, 1995.
[17] M. Hammer and D. Schweitzer, "Quantitative reflection spectroscopy at the human ocular fundus," *Phys. Med. Biol*., vol. 47, pp. 179–191, 2002.
[18] R. R. Anderson and J. A. Parrish, "The optics of human skin," *J. Invest. Dermatol*., vol. 77, pp. 13–19, 1981.
[19] S. Takatani and M. D. Graham, "Theoretical analysis of diffuse reflectance from a two-layer tissue model," *IEEE Trans. Biomed. Eng*., vol. BME-26, no. 12, pp. 656–664, Dec. 1987.
[20] F. C. Delori, "Noninvasive technique for oximetry of blood in retina vessels," *Appl. Opt*., vol. 27, pp. 1113–1125, 1988.
[21] D. J Faber, M. C. G. Aalders, E. G. Mik, B. A. Hooper, M. J. C. van Gemert, and T. G. van Leeuwen, "Oxygen saturation-dependent absorption and scattering of blood," *Phys. Rev. Lett*., vol. 93, pp. 028102-1–028102-4, 2004.
[22] J. A. Nelder and R. Mead, "A simplex method for function minimization," *Comput. J*., vol. 7, pp. 308–313, 1964.
[23] J. C. Ramella-Roman, S. A. Mathews, H. Kandimalla, A. Nabili, D. D. Duncan, S. A. D'Anna, S. M. Shah, and Q. Q. Nguyen, "Measurement of oxygen saturation in the retina with a spectroscopic sensitive multi aperture camera," *Opt. Exp*., to be published.

Jessica C. Ramella-Roman received the B.S. degree (Laurea) from the University of Pavia, Pavia, Italy, in 1993, and the M.S. and Ph.D. degrees from Oregon Health Science University, Portland, in 2004, all in electrical engineering.

She was a Postdoctoral Fellow at the Applied Physics Laboratory, Johns Hopkins University, Baltimore, MD. In 2006, she joined the Catholic University of America, Washington, DC, where she is currently an Assistant Professor of biomedical engineering. Her current research interests include polarized light imaging and modeling, the use of spectroscopic methodologies for measurements of skin and retinal oxygenation, and the design of fiber-optic probes for biomedical applications.

Scott A. Mathews (M'02) received the B.S. degree in physics in 1988, and the M.S. and Ph.D. degrees in materials engineering in 1994 from the University of Maryland, College Park, in 1993 and 2004, respectively.

He is currently an Assistant Professor of electrical engineering at the Catholic University of America, Washington, DC, where he is also the Director of the Laser Microfabrication Laboratory. His current research interests include laser materials processing, laser microfabrication, and microfluidic systems for biodetection.

Dr. Mathews has been the Faculty Advisor for the IEEE Student Chapter at the Catholic University of America since 2003.